Splenic extramedullary granulopoiesis and tissue microenvironments shape functionally distinct neutrophil subsets in autoimmunity

Guan Yang

gyang25@cityu.edu.hk

Department of Infectious Diseases and Public Health, City University of Hong Kong
https://orcid.org/0000-0002-2131-8435

Qianling Jiang
Department of Infectious Diseases and Public Health, City University of Hong Kong

Gaochen Zhu
Department of Infectious Diseases and Public Health, City University of Hong Kong

Wen Si
Department of Infectious Diseases and Public Health, City University of Hong Kong

Xin Ma
Department of Infectious Diseases and Public Health, City University of Hong Kong

Qiang Liu
Department of Neurology, Tianjin Medical University General Hospital, Tianjin 300052, China

Article

Keywords: Autoimmunity, neutrophil heterogeneity, functional reprogramming, multiple sclerosis

Posted Date: March 18th, 2026

DOI: https://doi.org/10.21203/rs.3.rs-9122986/v1

License: This work is licensed under a Creative Commons Attribution 4.0 International License.
Read Full License

Additional Declarations: There is no conflict of interest

Abstract

Neutrophils are increasingly recognized as key regulators of autoimmune responses and exhibit substantial functional diversity. However, the understanding of neutrophil heterogeneity in autoimmune diseases remains limited. Here, using experimental autoimmune encephalomyelitis (EAE), we identify three morphologically and transcriptionally distinct neutrophil subsets with tissue-specific distributions. Trajectory analysis reveals a stepwise maturation from proliferative precursors (N0) to immature (N1) and mature neutrophils (N2), with Ki67^{+}, Acvrl1^{+}, and CD300ld^{+} identified and validated as subset markers, respectively. Notably, pro-inflammatory CD300ld^{-} immature neutrophils preferentially infiltrate the central nervous system, whereas immunosuppressive CD300ld^{+} mature neutrophils expand in the lung during EAE. Mechanistically, splenic extramedullary granulopoiesis contributes to the expansion of the neutrophil pool, while disease-associated and tissue-specific microenvironments reshape their functional states. In addition, we identify previously uncharacterized subclusters within mature neutrophils, suggesting that autoimmune disease may generate distinct developmental lineages and expand the established architecture of the neutrophil compartment. Importantly, analogous neutrophil subsets are identified in mouse models of rheumatoid arthritis and systemic lupus erythematosus, with immature neutrophil infiltration into target tissues, while neutrophil subset reprogramming is also observed in patients with multiple sclerosis. Collectively, these findings show that splenic extramedullary granulopoiesis drives neutrophil heterogeneity and, together with tissue microenvironments, shapes their functional plasticity in autoimmunity, providing a framework for targeting defined subsets for immunomodulation.

Introduction

Multiple sclerosis (MS) is the most prevalent demyelinating disease of the central nervous system (CNS), characterized by immune-mediated demyelination. Its pathogenesis involves a complex interplay of different immune cells. Studies in patients with MS and its animal model, experimental autoimmune encephalomyelitis (EAE), have primarily emphasized the roles of T and B cells, which drive pathology both in the periphery and within the CNS. These lymphocytes contribute to CNS inflammation through diverse mechanisms, including promoting the recruitment of circulating myeloid cells such as neutrophils [1]. Neutrophils have long been considered a homogeneous population, yet accumulating evidence reveals their substantial phenotypic heterogeneity and functional versatility, especially in tumor contexts [2–6]. Nevertheless, comprehensive analyses of neutrophil heterogeneity in autoimmunity remain limited. Although historically overlooked due to their short lifespan, neutrophils are increasingly recognized as multifaceted participants in CNS autoimmunity [7]. In MS and EAE, they can aggravate disease by compromising the blood-brain barrier, supporting encephalitogenic Th17 cell development, generating reactive oxygen species, and releasing inflammatory mediators and neutrophil extracellular traps [8]. Intriguingly, they can exert protective effects by inhibiting T-cell proliferation and restraining the accumulation of pathogenic B cells within inflamed CNS tissue, where they are often described as polymorphonuclear myeloid-derived suppressor cells (PMN-MDSCs) [9,10]. Comparable pro- and anti-

inflammatory properties of neutrophils have also been described in other autoimmune diseases, including systemic lupus erythematosus and rheumatoid arthritis [11], underscoring their broader relevance. This raises the possibility that their opposing effects in MS/EAE and other autoimmune diseases may be attributed to their phenotypic heterogeneity.

Myeloid leukocytes are inherently capable of dynamic transcriptional and functional adaptation in response to local environmental cues. While these tissue-specific programs have been extensively characterized in macrophages, it remains largely unexplored whether neutrophils exhibit similar tissue-tailored behaviors. Emerging evidence indicates that neutrophils can indeed adopt diverse functional states dictated by their microenvironment, ranging from pro-inflammatory and NETotic to reparative or regulatory phenotypes [3,12,13]. However, how neutrophils are reprogrammed in autoimmune diseases and across distinct tissue environments remain poorly understood. A deeper understanding of these processes will shed light on how neutrophils contribute to disease pathogenesis and may uncover potential targets for therapeutic intervention.

Here, we comprehensively characterized neutrophil heterogeneity in autoimmune diseases and found that it underlies their divergent roles. Meanwhile, neutrophils exhibit remarkable diversity and undergo distinct transcriptional reprogramming across tissues and disease states. Together, our study delineates the molecular and functional landscape of neutrophil subsets in autoimmunity, providing valuable insights into their roles in disease pathogenesis and potential therapeutic targeting.

Results

Neutrophils exhibit tissue-specific functional states, nuclear morphology, and transcriptional diversity in EAE

To investigate the involvement of neutrophils in a murine model of MS, C57BL/6 mice were immunized with myelin oligodendrocyte glycoprotein peptide 35–55 (MOG_{35-55}) to induce EAE. Consistent with previous studies on neutrophil dynamics during EAE [14,15], we observed a marked expansion of $Ly6G^+$ $Ly6C^{low}$ neutrophils in multiple tissues including the spleen, bone marrow, brain, and spinal cord of EAE mice (fig. S1, A and B). In contrast, the frequency and absolute number of $Ly6C^{high}$ $Ly6G^-$ monocytes were much lower compared to neutrophils and showed no substantial difference between CFA and EAE groups (fig. S1C). We also examined neutrophil abundance in the lung, as increasing evidence has revealed an important role of the lung in shaping CNS autoimmunity [16–18]. Interestingly, we observed a substantial expansion of neutrophils but not monocytes in the lungs of EAE mice (fig. S1, A and C).

Neutrophils have been reported to exhibit both immunosuppressive and pro-inflammatory functions in MS/EAE [15,19,20]. To investigate these dual roles, we co-culture neutrophils isolated from the spleen, lung, and bone marrow of EAE mice at peak stage with CFSE-labeled naive $CD4^+$ T cells, or with naïve $CD4^+$ T cells under Th17-polarizing conditions. Neutrophils from all three tissues suppressed $CD4^+$ T cell

proliferation (Fig. 1A). Intriguingly, lung-derived neutrophils also inhibited Th17 cell differentiation, whereas spleen- and bone marrow-derived neutrophils promoted Th17 cell differentiation (Fig. 1A). Based on these findings, we speculated that tissue-specific neutrophil heterogeneity may underlie their functional divergence. To assess neutrophil heterogeneity, we first examined neutrophil morphology in different tissues. Neutrophils were classified into round-, banded-, and segmented-nucleus populations according to conventionally recognized nuclear morphology, corresponding to pre-neutrophils, immature neutrophils, and mature neutrophils, respectively [21]. Neutrophils isolated from the spleen and bone marrow of EAE mice showed similar distributions, with approximately 15–20% round, 30% banded, and 50–55% segmented cells, whereas lung-derived neutrophils were predominantly segmented (Fig. 1B). Collectively, these data indicate that neutrophils exhibit distinct tissue-specific heterogeneity at the morphological level, which may contribute to their divergent functional properties.

To comprehensively characterize neutrophil heterogeneity in EAE, we performed single-cell RNA sequencing of immune cells from the spleen, lung, and bone marrow of EAE mice at the peak stage. Seurat analysis identified 11 main cell types, which were manually annotated using canonical markers (Fig. 1C and fig. S2A). We next extracted the neutrophil population from the combined dataset and performed independent dimensionality reduction and clustering. Initial unsupervised clustering of neutrophils revealed five distinct clusters (fig. S2B). While minor transcriptional differences were noted between clusters 1 and 2, as well as between clusters 3 and 4, we consolidated the five clusters into three major subsets-N0 (cluster 0), N1 (clusters 1 and 2), and N2 (clusters 3 and 4)-based on overall gene expression patterns (Fig. 1D, and fig. S2C). Analysis of the distributions of these three neutrophil subsets revealed distinct tissue-specific patterns (Fig. 1D). N0 neutrophils were detected in the spleen (16.3%) and bone marrow (14.1%) but were nearly absent in the lung (0.4%) (Fig. 1D). N1 neutrophils were primarily found in the spleen (34.9%) and bone marrow (31.3%) (Fig. 1D). By contrast, N2 neutrophils were abundant across all tissues, comprising 48.5%, 96.2%, and 53.8% of neutrophils in the spleen, lung, and bone marrow, respectively (Fig. 1D).

To delineate the developmental trajectory of the identified neutrophil subsets, we first categorized them into the respective cell cycle states. N0 neutrophils displayed the highest proportion of cells in the S and G2M phase, indicating their early-stage and proliferative nature (Fig. 1E). Given that N0 neutrophils represent an early-stage and highly proliferative population, it was designated as the root for Monocle computational trajectory analysis on UMAP embeddings, which confirms a sequential pseudo-time trajectory from N0 to N1 and then to N2 neutrophils (Fig. 1E). Consistently, maturation and apoptosis scores increased progressively from N0 to N1 and N2 neutrophils (Fig. 1F), based on the expression of neutrophil maturation- and apoptosis-associated genes (table S1) [22]. We next compared our data with the neutrophil populations reported by Ng et al. [3], of which proNeu corresponded to our N0 neutrophils, IMM1 and IMM2 corresponded to our N1 neutrophils, and MAT1-MAT5 aligned with our N2 neutrophils (fig. S2D). Together, these results suggest that our N0, N1, and N2 neutrophils represent neutrophil precursors, immature neutrophils, and mature neutrophils, respectively. To further define the functional characteristics of each neutrophil subset, we performed Gene Ontology (GO) enrichment analysis based

on their differentially expressed genes (DEGs) (table S2). N0 neutrophils were primarily enriched in pathways related to the cell cycle, N1 neutrophils were associated with neutrophil activation and regulation of angiogenesis, whereas N2 neutrophils were enriched in immune response regulation (Fig. 1G). These findings highlight the distinct functional specializations among these subsets.

To extend our analysis beyond peripheral tissues, we next examined neutrophil heterogeneity within the CNS. Publicly available single-cell transcriptomic datasets of CNS immune cells were analyzed [23,24], and our N0, N1, and N2 labels were mapped onto neutrophils identified by *S100a8*, *S100a9*, and *Ly6g* expression (fig. S2, E and F). Notably, N0 and N1 neutrophils were also present in the CNS, accounting for approximately 14% and 20% of CNS neutrophils, respectively (Fig. 1H). Morphological analysis further confirmed the presence of these subsets in the CNS of EAE mice (Fig. 1I). Collectively, our results demonstrate that neutrophils in EAE exhibit tissue-specific heterogeneity and comprise three subsets that are morphologically and transcriptionally distinct.

Identification of subset-defining markers and characterization of functionally distinct neutrophil subsets in EAE

Next, we sought to identify markers that could characterize the three neutrophil subsets. We found that *Mki67*, *Acvrl1*, and *Cd300ld* were predominantly expressed in the N0, N1, and N2 neutrophils, respectively (Fig. 2A). Ki67 (encoded by *Mki67*) is a well-established proliferation marker, and its high expression reflects the proliferating status of N0 neutrophils. Acvrl1 (encoded by *Acvrl1*) is a transmembrane serine/threonine receptor kinase belonging to the transforming growth factor-β receptor family, primarily expressed on endothelial cells [25]; however, its role in neutrophils remains unclear. CD300ld (encoded by *Cd300ld*) is a single-pass transmembrane protein in the CD300 family, recently identified as a critical immune suppressor present on pathologically activated neutrophils and implicated in their recruitment [26]. We next profiled expression of these three markers in neutrophils from different tissues of EAE mice by flow cytometry. In the spleen and bone marrow of EAE mice, Ki67$^+$, Acvrl1$^+$, and CD300ld$^+$ neutrophils accounted for approximately 18–19%, 30%, and 50–60% of the total neutrophil population, respectively (Fig. 2B). In contrast, CD300ld$^+$ neutrophils accounted for approximately 97%, 86%, 70%, and 69% of neutrophils in the lung, blood, spinal cord, and brain, respectively (Fig. 2B). These proportions were consistent with our morphological and single-cell transcriptomic analyses (Fig. 1, B and D). To further validate CD300ld as a marker of mature N2 neutrophils, we examined the morphology of CD300ld$^+$ and CD300ld$^-$ neutrophils. CD300ld$^+$ neutrophils displayed typical mature morphology with segmented nuclei, whereas CD300ld$^-$ neutrophils exhibited round and banded nuclei (Fig. 2C). In line with these findings, CD300ld$^+$ neutrophils consistently co-expressed the maturation marker CD101 and the chemokine receptor CXCR2 (Fig. 2D) [27] and had a higher apoptotic rate than CD300ld$^-$ neutrophils (Fig. 2E), further confirming their mature status. Together, these findings support the use of Ki67, Acvrl1, and CD300ld as markers to distinguish N0, N1, and N2 neutrophil subsets.

Immunofluorescence staining of the spleen, lung, and bone marrow of EAE mice at peak stage confirmed that most neutrophils in the lung were CD300ld^{+}, whereas only a subset of neutrophils in the spleen and bone marrow expressed CD300ld (Fig. 2F). Notably, CD300ld^{+} and CD300ld^{-} neutrophils exhibited distinct spatial distributions. In the spleen, CD300ld^{+} neutrophils were primarily located in the marginal zone and formed clusters, while CD300ld^{-} neutrophils were also enriched in the red pulp (Fig. 2F). In the lung, CD300ld^{+} neutrophils distributed throughout the interstitial regions (Fig. 2F). In the bone marrow, CD300ld^{+} neutrophils were predominantly localized near the central vascular region (Fig. 2F). These observations indicate that neutrophil subsets display tissue- and subset-specific spatial organization, which may contribute to their functional divergence in EAE.

To investigate which subset may possess immunosuppressive activities, we performed a gene scoring analysis based on established MDSC gene signature (table S1) [4] and found that N2 neutrophils exhibit the highest MDSC score among the three subsets (Fig. 2G). Prior studies have identified multiple neutrophil subsets with immunosuppressive functions, including CD14^{high}, CD84^{high}, FasL^{+} PD-L2^{+}, CD16^{high} CD62L^{dim}, and CD10^{+} ALPL^{+} populations [2,4,28–30]. While N2 neutrophils displayed low expression of *Fasl* (encoding FasL), *Mme* (encoding CD10), and *Alpl* (encoding ALPL), along with sustained expression of *Sell* (encoding CD62L), it nevertheless shared key molecular features with previously described populations, including elevated expression of *Cd14* (encoding CD14), *Cd84* (encoding CD84), *Pdcd1lg2* (encoding PD-L2), and *Fcgr3* (encoding CD16) (Fig. 2H). These results suggest that N2 neutrophils represent the immunosuppressive population. Additionally, the frequency of CD300ld^{+} neutrophils from the spleen of EAE mice negatively correlated with CD4^{+} T cell proliferation in our *in vitro* co-culture (Fig. 2I). Meanwhile, CellChat analysis revealed strong interactions between CD4^{+} T cells and neutrophil subsets during EAE, with N2 neutrophils displaying particularly high interaction strength (Fig. 2J). To functionally validate the immunosuppressive activity of CD300ld^{+} neutrophils, we isolated these cells from the spleens of EAE mice and tested their ability to suppress the proliferation of CD4^{+} T cells. We found that CD300ld^{+} neutrophils from spleens of EAE mice showed greater immunosuppression on CD4^{+} T cell proliferation compared with CD300ld^{-} neutrophils (Fig. 2K). Given that Arginase1 (encoded by *Arg1*) and NO (generated from inducible NO synthase, *Nos2*) are major contributors to MDSC immune suppressive activities [31], we compared their expression between subsets by quantitative polymerase chain reaction (qPCR). CD300ld^{+} neutrophils expressed significantly higher level of *Nos2* than CD300ld^{-} neutrophils, whereas *Arg1* expression was low overall and did not differ between subsets (Fig. 2L). Notably, unlike total Ly6G^{+} or CD300ld^{-} neutrophils, which promoted Th17 differentiation, CD300ld^{+} neutrophils lacked this capacity (Fig. 2M), underscoring their distinct functional profile. Together, these findings provide a mechanistic explanation for the tissue-specific functional divergence of neutrophils in EAE.

Splenic extramedullary granulopoiesis contributes to neutrophil heterogeneity in EAE

Our data revealed a marked expansion of neutrophils in the spleen, lung, and CNS of EAE mice compared with CFA-immunized controls (fig. S1, A and B). Notably, neutrophil numbers in the spleen exceeded those in the bone marrow during EAE (fig. S1A), suggesting that the spleen may serve as an additional site of neutrophil production under autoimmune conditions. Given that the spleen is a known site of extramedullary granulopoiesis [32], we next examined whether this process occurs during EAE. Trajectory analysis revealed a continuous neutrophil developmental program in the bone marrow (Fig. 3A). A similar trajectory was observed in the spleen but was absent in the lung (Fig. 3A), indicating that EAE induces splenic extramedullary granulopoiesis.

Extramedullary hematopoiesis is extremely rare in the lung [33] and that neutrophils in the CNS are recruited from peripheral tissues. To determine the possible origin of these accumulated neutrophils, we performed Pearson correlation analysis. Lung neutrophil subsets exhibited transcriptional profiles more closely resembling those of spleen neutrophil subsets than those of bone marrow subsets (Fig. 3B). In addition, we examined retention and egress markers [34,35] in N2 neutrophils from the three tissues of EAE mice. Notably, spleen-derived N2 neutrophils expressed higher levels of the retention marker *Cxcr4* and *Itga4*, as well as the egress marker *Cxcr2* (Fig. 3C). Flow cytometric analysis revealed that splenic CD300ld$^+$ neutrophils exhibited the highest CXCR2 expression among all tissues examined, followed by bone marrow-derived, whereas CXCR2 levels were relatively low on neutrophils from the lung, brain, and spinal cord (Fig. 3D), suggesting that splenic N2 neutrophils may be the major contributors to the expanded neutrophil pool in the periphery and CNS. By contrast, CD300ld$^+$ neutrophils in the brain and spinal cord displayed high CXCR4 expression but low levels in the spleen and bone marrow (Fig. 3E), consistent with their retention within the CNS. We next examined the expression of neutrophil-attracting chemokines, including *Cxcl1*, *Cxcl2*, and *Cxcl5* [36]. Among these, *Cxcl2* was highly expressed by neutrophils, monocytes, and tissue-resident macrophages in the lungs of EAE mice, whereas *Cxcl1* and *Cxcl5* were consistently low (fig. S3A), suggesting that CXCL2 may serve as the predominant chemokine mediating neutrophil recruitment to the lung. Together, these findings indicate that the migration of splenic N2 neutrophils to other sites during EAE is likely mediated via the CXCR2-CXCL2 axis.

To assess whether the EAE-induced splenic extramedullary granulopoiesis contributes to neutrophil heterogeneity in EAE mice, we injected CFSE and CellTrace Violet (CTV) into the bone marrow and spleen of EAE mice, respectively, to track neutrophil migration [37]. Five hours later, labeled neutrophils were detected in the blood, spleen, bone marrow, and lung (fig. S3B). Spleen- and bone marrow-derived neutrophils accumulated in the lungs to a comparable extent (Fig. 3F), suggesting that both tissues contribute equally to the lung neutrophil accumulation during EAE. Interestingly, we also observed reciprocal trafficking of neutrophils between the spleen and bone marrow, with a greater number of bone marrow-derived neutrophils migrating to the spleen compared to the spleen-derived neutrophils migrating to the bone marrow (fig. S3B). We further examined the subset composition of spleen-derived neutrophils migrating to the bone marrow, lung, and blood and found that approximately 70%, 90% and 60% were CD300ld$^+$, respectively (Fig. 3G). These results indicate that spleen-derived neutrophils contribute both to the pool of precursor and immature neutrophils in the circulation and to the

accumulation of mature neutrophils in the lung. Together, these findings suggest that splenic extramedullary granulopoiesis represents an additional source contributing to neutrophil heterogeneity in EAE mice.

EAE reshapes neutrophil subset functions

Next, we investigated whether neutrophils from naïve mice also exhibit tissue-specific functional states, nuclear morphology, and transcriptional diversity. To this end, neutrophils isolated from the spleen, lung, and bone marrow of naïve mice were co-cultured with naïve $CD4^+$ T cells, either under non-polarizing conditions or under Th17-polarizing conditions. In contrast to EAE-derived neutrophils, spleen- and bone marrow-derived neutrophils from naïve mice failed to suppress $CD4^+$ T cell proliferation (Fig. 4A). Notably, lung-derived neutrophils retained the capacity to inhibit $CD4^+$ T cell proliferation (Fig. 4A). Moreover, lung-derived neutrophils also suppressed Th17 cell differentiation, whereas spleen- and bone marrow-derived neutrophils no longer promoted Th17 differentiation under the same conditions (Fig. 4A). We next examined the nuclear morphology of neutrophils from naïve mice. Neutrophils isolated from the spleen and lung were predominantly characterized by segmented nuclei, indicating a largely mature population (Fig. 4, B and C). In contrast, bone marrow-derived neutrophils displayed marked morphological heterogeneity, with approximately 20% exhibiting round nuclei, 30% showing band-shaped nuclei, and 50% presenting segmented nuclei (Fig. 4, B and C). This distribution is consistent with active granulopoiesis in the bone marrow under steady-state conditions, encompassing precursor, immature, and mature neutrophil stages. To further explore subset composition, we integrated publicly available scRNA-seq datasets from the spleen [38,39], lung [40,41], and bone marrow [39] of naïve C57BL/6 mice to examine the tissue distribution of our previously defined neutrophil subsets. We observed marked tissue-specific differences in subset composition. N0 neutrophils were enriched in the spleen (27.5%) and bone marrow (14.9%) but were relatively rare in the lung (7.8%) (Fig. 4D). N1 neutrophils were most abundant in the bone marrow (34.5%), with lower frequencies in the spleen (9.7%) and lung (14.4%) (Fig. 4D). In contrast, N2 neutrophils constituted the dominant population across all examined tissues, accounting for 62.8% in the spleen, 77.8% in the lung, and 50.6% in the bone marrow (Fig. 4D). Although the subset proportions in the bone marrow of naïve mice were similar to those observed under EAE condition (Fig. 1D), their functional profiles were strikingly different (Fig. 1A and 4E), indicating that subset proportion alone does not predict neutrophil function and suggesting that EAE induces functional reprogramming.

We next examined how EAE induction alters neutrophil subset functions across tissues. Comparisons of each neutrophil subset between EAE and naïve mice within individual tissues revealed extensive gene expression changes (Fig. 4E) (table S3). In the spleen and bone marrow, N0 neutrophils from EAE mice were enriched for myeloid cell differentiation pathways (Fig. 4F), consistent with EAE-driven granulopoiesis initiating at early developmental stages in these tissues (Fig. 3A). In N1 neutrophils, EAE enhanced chemotaxis-related pathways in the spleen and lung, as well as translation-associated signatures in the bone marrow (Fig. 4F), suggesting increased migratory capacity and biosynthetic

activity. N2 neutrophils were enriched for immune response-related pathways across tissues (Fig. 4F), suggesting an enhanced involvement in immune response regulation during EAE. Collectively, these results demonstrate that EAE drives functional reprogramming of neutrophil subsets.

Tissue-specific reprogramming of neutrophil subsets in EAE

Myeloid leukocytes can acquire phenotypic and transcriptional profiles unique to their tissue of residence, a feature well characterized in macrophages but less studied in neutrophils. To further investigate tissue-specific reprogramming in neutrophil subsets during EAE, we performed GO analysis on upregulated DEGs (table S4). N0 neutrophils were enriched for myeloid cell differentiation in the spleen, translation-related pathways in the lung, and Golgi vesicle transport in the bone marrow (Fig. 5A). N1 neutrophils exhibited enrichment for translation in the spleen, immune response regulation in the lung, and RNA splicing in the bone marrow (Fig. 5A). N2 neutrophils were enriched for translation in the spleen, immune response regulation in the lung, and actin filament organization in the bone marrow (Fig. 5A), suggesting that neutrophils in the lung may adopt more immunomodulatory functions compared to those in other tissues.

To further determine whether microenvironment contributes to the acquisition of immunosuppressive features, we first compared the expression of genes related to immunosuppression [42]. Lung-derived N2 neutrophils displayed higher expression of *Ptgs2*, *Il1b*, *Arg2*, *Nos2*, *Cd274*, *Trem1*, *Fas*, *Pdcd1lg2*, *Cd14*, *Clec4d*, *Clec4e*, *C5ar1*, *Fasl*, *Mme*, and *Cd300ld* compared with their bone marrow or spleen counterparts (Fig. 5B). We next assessed the expression of two key immunosuppressive markers, CD300ld and PD-L1, within the CD300ld$^+$ neutrophils by flow cytometry. CD300ld expression was highest in lung-derived CD300ld$^+$ neutrophils relative to those from other tissues (Fig. 5C), consistent with their pronounced immunosuppressive transcriptional profile. Interestingly, although lung-derived CD300ld$^+$ neutrophils exhibited a modest increase in the frequency of PD-L1$^+$ cells compared to those from the spleen and bone marrow, the highest PD-L1 expression was observed in CD300ld$^+$ neutrophils from the brain, followed by the spinal cord (Fig. 5D), suggesting that the CNS microenvironment may further shape neutrophil functional states. Finally, to directly test whether the lung microenvironment actively drives this immunosuppressive reprogramming, we analyzed CD300ld expression in our *in vivo* cell tracing assay (Fig. 3G). The results showed a slight trend toward reduced CD300ld expression in splenic and bone marrow-derived CD300ld$^+$ neutrophils upon entering the blood, whereas CD300ld expression was significantly upregulated following migration to the lung (Fig. 5E). Collectively, these results demonstrate that tissue-specific microenvironments, particularly the lung, actively reprogram neutrophil subsets toward distinct immunosuppressive states during EAE.

Refined dissection of neutrophil subsets uncovers heterogeneity within N0, N1, and N2 populations

Our classification of neutrophils into N0, N1, and N2 subsets corresponds to the precursor, immature, and mature stages, respectively. However, recent studies have demonstrated that neutrophils comprise multiple transcriptionally and functionally distinct populations, with reported subdivisions ranging from 3 to 11 subsets [2–5]. To determine whether the functional differences observed between neutrophil subsets in EAE and naïve mice, as well as tissue-specific variations, are associated with changes in the frequency of sub-clusters, we integrated datasets from EAE and naïve mice and performed in-depth subclustering analyses of the N0, N1, and N2 subsets. Unsupervised analysis further subdivided N0 neutrophils into three sub-clusters, defined by the expression of *Elane*, *Mmp9*, and *Btnl10* (Fig. 6A, and fig. S4A), which follow a developmental trajectory from *Btnl10*$^+$ to *Elane*$^+$, and then to *Mmp9*$^+$ cells (Fig. 6A). *Btnl10*$^+$ cells were predominantly enriched in the naïve spleen, EAE spleen, and EAE lung, and were associated with translation-related processes (Fig. 6, B and C). *Elane*$^+$ cells represented the dominant population within N0 neutrophils, with the highest proportion observed in the EAE lung, and were enriched for pathways related to translation and DNA replication (Fig. 6, B and C). *Mmp9*$^+$ cells were primarily enriched in the EAE spleen and bone marrow, and showed enrichment for chemotaxis-related pathways (Fig. 6, B and C), suggesting that this sub-cluster may represent the population that migrates from the spleen and bone marrow into the circulation during EAE.

Similarly, N1 neutrophils were subdivided into three sub-clusters-*Mmp8*$^+$, *Fcnb*$^+$, and *Lta4h*$^+$-based on marker gene expression (Fig. 6D, and fig. S4B). These cells progress developmentally from *Fcnb*$^+$ to *Lta4h*$^+$, and finally to *Mmp8*$^+$ cells (Fig. 6D). Functionally, *Fcnb*$^+$ cells were enriched for translation-related processes, *Lta4h*$^+$ cells for small molecule catabolic processes, and *Mmp8*$^+$ cells for immune response-related pathways (Fig. 6E), highlighting distinct functional specializations of N1 sub-clusters. The proportion of *Lta4h*$^+$ cells remained relatively stable within each tissue (Fig. 6F), suggesting limited responsiveness to EAE induction. In contrast, *Fcnb*$^+$ cells increased across all three tissues upon EAE induction, whereas *Mmp8*$^+$ cells decreased in proportion (Fig. 6F).

Unsupervised clustering resolved N2 neutrophils into seven transcriptionally distinct subclusters: *Ngp*$^+$, *St3gal1*$^+$, *Cd74*$^+$, *Ccl4*$^+$, *Cstdc4*$^+$, *Stfa1*$^+$, and *Ifit1*$^+$ (Fig. 6G, and fig. S4C). Trajectory analysis indicated that *Ngp*$^+$ neutrophils represent an early shared state that converges on *St3gal1*$^+$ cells as a common intermediate, followed by divergence into three terminal branches characterized by *Cstdc4*$^+$/*Stfa1*$^+$ (Lineage 1), *Ccl4*$^+$ (Lineage 2), and *Cd74*$^+$ (Lineage 3) populations (Fig. 6G). Functional annotation highlighted distinct specializations among these sub-clusters: *Ccl4*$^+$ cells were enriched for immune response-related pathways, *Cd74*$^+$ cells for translation-associated programs, *Cstdc4*$^+$ and *Stfa1*$^+$ cells for peptide cross-linking processes, *Ifit1*$^+$ cells for antiviral responses, *Ngp*$^+$ cells for actin cytoskeleton-related functions, and *St3gal1*$^+$ cells for immune response-associated pathways (Fig. 6H). *St3gal*1$^+$ cells represented the major component of N2 neutrophils across all tissues and conditions (47–62%) (Fig. 6I). Notably, EAE conditions reshaped the composition of N2 sub-clusters, promoting differentiation toward lineage 1 (*Cstdc4*$^+$/*Stfa1*$^+$) and lineage 2 (*Ccl4*$^+$), while reducing the proportion of lineage 3 *Cd74*$^+$ neutrophils (Fig. 6I). Given that N2 neutrophils represent the mature neutrophil compartment, we next examined canonical neutrophil functional programs across N2 subclusters. Antibacterial activity scores were uniformly high across most sub-clusters, with the notable exception of *Cd74*$^+$ cells (Fig. 6J).

Functional scoring further revealed marked specialization: *Ngp*$^+$ cells exhibited elevated degranulation and ROS production, *Ccl4*$^+$ cells displayed the highest NETosis scores, *St3gal1*$^+$ cells showed enhanced phagocytic capacity, and chemotaxis scores were high across all sub-clusters except *Ngp*$^+$ cells (Fig. 6J). Notably, *Cd74*$^+$ cells showed the highest antigen-presenting cell (APC) scores, while immunosuppressive signatures were most prominent in *St3gal1*$^+$ and *Ccl4*$^+$ sub-clusters (Fig. 6J). Glycolytic activity was uniformly elevated across all N2 sub-clusters, and extravasation-related scores were high in all sub-clusters except *Cd74*$^+$ (Fig. 6J). In conclusion, the functional differences observed between neutrophil subsets in EAE and naïve mice, as well as across tissues, may largely reflect shifts in subcluster composition. EAE selectively expanded or reduced specific subclusters-such as *Mmp8*$^+$*/Fcnb*$^+$ in N1, and *Cstdc4*$^+$/*Stfa1*$^+$ and *Ccl4*$^+$ in N2-while others remained relatively stable. Notably, the composition of neutrophil sub-clusters in the lung differed from that in other tissues. These changes in sub-cluster abundance correspond to distinct functional programs, including chemotaxis, immune response, translational activity, and peptide cross-linking, indicating that EAE and tissue environment possibly reshapes neutrophil functions through modulation of subcluster distribution.

As our earlier observations indicated that mature N2 neutrophils exhibit the most extensive interactions with CD4$^+$ T cells (Fig. 2J), we next asked whether distinct N2 sub-clusters differ in their interactions with CD4$^+$ T cells. To address this, we performed CellChat analysis focusing on communication between N2 neutrophil sub-clusters and major CD4$^+$ T cell subsets, including Treg, CD4 effector, and CD4 naïve/memory cells (fig. S4D). Across all N2 sub-clusters, cell-cell interactions were predominantly mediated through the *Sirpb1-Cd47* axis (fig. S4E), indicating a conserved mechanism of neutrophil-T cell communication. In addition, *St3gal1*$^+$, *Ccl4*$^+$, and *Ifit1*$^+$ neutrophils showed prominent interactions via *Cd80-Ctla4*/*Cd28* (fig. S4E), suggesting a potential role in modulating T cell activation and costimulatory signaling. Notably, *Cd74*$^+$ neutrophils exhibited strong interactions with all three CD4$^+$ T cell subsets through MHC class II-CD4 signaling (fig. S4E), providing functional evidence for their antigen-presenting capacity. These results suggest that distinct N2 neutrophil sub-clusters engage CD4$^+$ T cells through specialized communication programs, potentially contributing to their functional heterogeneity in autoimmune settings.

Recent studies have established a comprehensive NeuMap across multiple tissues and conditions [6]. However, autoimmune contexts were not explored in these analyses. To address this gap, we transferred the labels of our neutrophil subclusters onto the NeuMap. We observed strong concordance for several populations: our *Cd74*$^+$ N2 neutrophils mapped to the *H2*$^+$ *Cd74*$^+$ subset, and our *Ifit1*$^+$ N2 neutrophils aligned with their *Ifit1*$^+$ neutrophils. Additionally, our *Elane*$^+$ and *Mmp9*$^+$ N0 neutrophils corresponded to their *Ltf*$^+$ *Mki67*$^+$ population, confirming their identity as progenitor-like cells. Similarly, our *Fcnb*$^+$, *Lta4h*$^+$, *Mmp8*$^+$ N1 neutrophils aligned with their *Cebpb*$^+$ *Mmp8*$^+$ subset, consistent with an immature neutrophil state. In contrast, we also identified notable differences. Their *Cd14*$^+$ *Ptgs2*$^+$ and *Cd52*$^+$ populations corresponded to our *St3gal1*$^+$ N2 neutrophils. Our *Ccl4*$^+$, *Stfa1*$^+$, *Cstdc4*$^+$ N2 neutrophils were rarely detected in their dataset, indicating that autoimmune conditions may involve previously uncharacterized

neutrophil subclusters and developmental lineages (Fig. 6K). Overall, these findings broaden the existing NeuMap and highlight additional layers of neutrophil heterogeneity under autoimmune settings.

Conserved neutrophil subsets across autoimmune diseases

To assess the conservation of neutrophil subsets across autoimmune diseases, we reanalyzed publicly available datasets from the collagen-induced arthritis (CIA) [43] and SLE.yaa mice [44,45]. Similar to EAE, the CIA model is antigen-adjuvant-driven and contains three analogous neutrophil subsets: *Mki67*$^{+}$ N0, *Acvrl1*$^{+}$ N1, and *Cd300ld*$^{+}$ N2 neutrophils (Fig. 7A). Remarkably, SLE.yaa mice, which develop spontaneous severe glomerulonephritis, also exhibited these three subsets (Fig. 7B). Interestingly, we also detected N0 and N1 neutrophils infiltrating the affected tissues, such as joints and kidneys, in these autoimmune models (Fig. 7C). This pattern is similar to what has been observed in EAE (Fig. 1, H and I). These observations raise the possibility that splenic extramedullary granulopoiesis contributes to the accumulation of precursor and immature neutrophils in diseased tissues across multiple autoimmune diseases.

To determine whether these neutrophil subsets are conserved in human autoimmunity, we next examined our previously published scRNA-seq data from the bone marrow of patients with MS [46]. We also identified three distinct neutrophil subsets (Fig. 7D). Similar to the EAE model, N0 neutrophils from patients with MS and healthy controls had the highest proportion of cells in the S/G2M phases, reflecting their early proliferative state (Fig. 7D). These neutrophils also followed a conserved maturation trajectory that progressed sequentially from N0 to N1 and then to N2 neutrophils (Fig. 7D). As in the bone marrow of EAE mice, the proportions of these three subsets did not differ significantly between healthy controls and patients with MS (Fig. 7E). In addition, comparison of neutrophil subsets between patients with MS and healthy controls revealed that N0 neutrophils in patients with MS were more enriched for biogenesis-related processes (Fig. 7F), consistent with the enhanced granulopoiesis we previously observed [46]. N1 neutrophils in MS showed increased engagement in antimicrobial responses, while N2 neutrophils were more involved in phagocytosis and neutrophil activation (Fig. 7F). These results collectively indicate the conservation of neutrophil subsets and suggest functional reprogramming of neutrophils in patients with MS.

Discussion

Neutrophils are traditionally regarded as homogeneous, short-lived effectors of the innate immune system. However, recent advances in single-cell technologies have firmly established that neutrophils are not a homogeneous population but instead comprise phenotypically and transcriptionally distinct subsets with specialized effector programs. For example, studies in murine models of transplantable Lewis lung carcinoma, pancreatic cancer, breast cancer, and brain tumors have identified 3–11 neutrophil populations [2–5], and infection models such as trypanosomiasis and *Escherichia coli* also revealed several transcriptionally distinct clusters [22,39]. These findings underscore the remarkable

plasticity of neutrophils in different pathological settings. While efforts have been made to classify neutrophils into numerous subsets, overly fine distinctions often yield limited insights and complicate interpretation. A recent review highlighted the need for a standardized framework and proposed a four-tiered system for neutrophil classification, encompassing developmental stages, functional modules, defining identifiers, and tissue localization [13]. Building on this concept, we combined morphological analysis with single-cell transcriptomics and identified three distinct neutrophil subsets: a proliferative precursor population (N0 neutrophils), which differentiates into an intermediate immature subset (N1 neutrophils), and ultimately matures into a terminal subset (N2 neutrophils). This developmental trajectory is observed in the bone marrow and spleen of EAE mice, whereas it is not evident in the lung. These findings align with the classical model of neutrophil development, wherein the bone marrow serves as the primary site of granulopoiesis, while the spleen acts as an auxiliary site under inflammatory conditions [32].

Previous studies have used CXCR2 and CD101 as markers of neutrophil maturation [27,47]; however, these markers do not sufficiently resolve the continuum of neutrophil development. Here, we establish Ki67, Acvrl1, and CD300ld as defining identifiers of three transcriptionally and morphologically distinct neutrophil populations, corresponding to progressive stages of neutrophil differentiation. This marker-based framework enables a more precise dissection of neutrophil developmental heterogeneity across tissues and disease contexts. Another important finding is the infiltration of neutrophil precursors and immature neutrophils into major target tissues in autoimmune diseases, including the CNS, joints, and kidneys, highlighting their potential contribution to disease progression. The presence of neutrophil precursors and immature neutrophils in these tissues may reflect both bone marrow-derived and splenic extramedullary granulopoiesis under inflammatory conditions, suggesting that autoimmune inflammation promotes recruitment of early-stage neutrophils beyond classical mature populations. Although the functions of immature neutrophils remain incompletely understood, previous studies indicate that they retain key innate immune capabilities, such as bacterial phagocytosis and killing via reactive oxygen species, although less efficiently than mature neutrophils [48]. Moreover, there is growing evidence that immature neutrophils can contribute to tissue injury under both infectious and inflammatory conditions [49–51]. Consistent with these observations, we note that CD300ld^{-} neutrophils in EAE mice tend to promote Th17 cell differentiation, suggesting a potential role in driving pro-inflammatory responses. These findings underscore the need to further study immature neutrophils in autoimmune disease and raise the possibility that modulating their accumulation or activity could provide new avenues for therapeutic intervention.

It is well established that macrophages [52] and lymphocytes [53–55] adapt to tissue environments, performing roles beyond their classical functions, including maintaining tissue homeostasis, responding to stress, and modulating pathological processes. Although neutrophils have been considered transcriptionally less active compared with other myeloid cells, growing studies highlight their rapid reprogramming in response to environmental signals [12,22]. Here, we found that lung-infiltrating neutrophils displayed a distinct transcriptional program compared to the spleen and bone marrow,

characterized by enrichment of cytokine-mediated signaling and immune-response pathways. This suggests that the lung microenvironment uniquely amplifies neutrophil functional activation. However, the mechanisms underlying this lung-specific neutrophil reprogramming remain poorly understood, though continuous exposure to microorganisms and environmental antigens may play a role. Recent study indicates that modulation of the lung microbiota can impact EAE development, suggesting that the pulmonary microbiome may shape systemic immune responses in autoimmunity [18]. Our findings broaden the concept of myeloid plasticity by demonstrating the adaptability of neutrophils across distinct tissue environments. In particular, lung neutrophils during autoimmunity displayed distinct transcriptional programs, pointing to opportunities for organ-specific therapeutic interventions. Future studies incorporating additional lymphoid and non-lymphoid tissues, and examining multiple disease stages will be critical to fully delineate how tissue microenvironments shape neutrophil diversification.

In summary, our study delineates distinct neutrophil subsets, their developmental trajectory, and reveals their differential distribution across tissues. We identify reliable markers to distinguish these subsets and uncover mechanisms underlying their functional plasticity. Meanwhile, we reveal splenic extramedullary granulopoiesis drives neutrophil heterogeneity, and disease- and tissue-specific reprogramming in autoimmunity. These findings provide a foundation for future strategies to selectively target neutrophils and advance precision therapies.

Materials and Methods

Mice and EAE induction

EAE induction was performed as previously described [56]. Briefly, 6-10-week-old C57BL/6 mice of both sexes were subcutaneously immunized with 200 µl of 2 mg/ml MOG_{35-55} peptide (MEVGWYRSPFSRVVHLYRNGK; Thermo Scientific) emulsified in Freund's complete adjuvant containing 2 mg/ml Mycobacterium tuberculosis H37Ra extract (BD Biosciences, 231141). Pertussis toxin (Calbiochem, 516560) was administered intraperitoneally at 400 ng per mouse on days 0 and 2 post-immunization. Control mice received either Freund's complete adjuvant alone (CFA controls) or no treatment (naïve controls). All animals were maintained under specific pathogen-free conditions in the Institutional Laboratory Animal Research Unit. Experimental procedures were approved by the Animal Ethics Committee of the City University of Hong Kong (AN-STA-00000146 and AN-STA-00001149) and conducted in accordance with institutional guidelines.

Mouse neutrophil isolation

Neutrophils were isolated from the spleen, lung, and bone marrow of naïve or EAE mice at the peak stage by positive selection using biotin-conjugated anti-mouse Ly6G antibodies (BioLegend, 127604; >90% purity). For isolation of CD300ld^{+} neutrophils, neutrophils were first enriched by negative selection using the Neutrophil Isolation Kit (Miltenyi Biotec, 130-097-658; >90% purity) according to the

manufacturer's instructions, followed by staining with PE-conjugated anti-mouse MAIR-IV antibody (BioLegend, 139605) and isolation using anti-PE MicroBeads (BioLegend, 480079; >95% purity).

T cell suppressive assay

Naïve $CD4^+$ T cells were purified from C57BL/6 spleens using the $CD4^+$ T Cell Isolation Kit (Miltenyi Biotec, 130-104-454; >95% purity) according to the manufacturer's instructions and labeled with CFSE (Invitrogen, C34554). Labeled $CD4^+$ T cells (1.5×10^5) were activated with plate-bound anti-CD3e (5 μg/ml; eBioscience, 16-0031-85) and soluble anti-CD28 (2 μg/ml; eBioscience, 16-0281-82) and co-cultured with neutrophils from naïve or peak-stage EAE mice at a 1:1 ratio for 48 hours. Proliferation of $CD4^+$ T cells was then assessed by flow cytometry.

Th17 differentiation assay

Naive $CD4^+$ T cells were stimulated with plate-bound anti-CD3e (2 μg/ml; eBioscience, 16-0031-85) and soluble anti-CD28 (1 μg/ml; eBioscience, 16-0281-82) in Th17-polarizing conditions containing IL-6 (20 ng/ml; PeproTech, 216 – 16), TGF-β (5 ng/ml; PeproTech, 100-21C), anti-IL-4 (5 μg/ml; BioLegend, 504122), and anti-IFN-γ (5 μg/ml; BioLegend, 505834), and then co-cultured with neutrophils from naïve or peak-stage EAE mice at a 1:1 ratio for 5 days. The proportion of Th17 cells was subsequently assessed by flow cytometry.

Wright-Giemsa staining

$Ly6G^+$ neutrophils, $CD300ld^+$ $Ly6G^+$ neutrophils, and $CD300ld^-$ $Ly6G^+$ neutrophils were isolated as mentioned above. Leukocytes from the brain and spinal cord were isolated following Percoll (Cytiva,17089101) density gradient centrifugation. Cells were cytocentrifuged onto glass slides. Slides were stained with the Diff-Quick Stain Set (Sigma, GS500), and then were observed using a Nikon Eclipse Ti2 microscope.

Flow cytometry

Mice were euthanized by lethal anesthesia, and spleen, lung, bone marrow, brain and spinal cord samples were collected. Spleen, bone marrow and spinal cord samples were mechanically dissociated and passed through a 70-μm strainer. Lungs and brains were minced and digested in HBSS supplemented with 5% FBS (Gibco, A5256801) and 0.04 mg/ml Collagenase Type I (Gibco, 17100017) at 37°C for 45 minutes, then mechanically disrupted and filtered through a 70-μm strainer. Cells were subjected to erythrocyte lysis using ACK lysing buffer (Gibco, A1049201) and subsequently resuspended to generate single-cell suspensions. For surface staining, cells were preincubated with normal rat serum to block Fc receptors, then stained with fluorochrome-conjugated antibodies against mouse CD45 (BioLegend, 103115), Ly6C (BioLegend, 128033), Ly6G (BioLegend, 127618), CD300ld (BioLegend, 139605), CXCR2 (BioLegend, 149309), CD101 (Miltenyi, 130-126-310), CXCR4 (BioLegend, 146511), PD-L1 (BioLegend, 124313), and CD4 (BioLegend, 100412). For intracellular cytokine staining, cells were stimulated with Cell Stimulation Cocktail (eBioscience, 00-4970-03) for 4 hours, followed by fixation and permeabilization using the BD Cytofix/Cytoperm™ Kit (BD Biosciences, 554714). Cells were then stained

with anti-IL-17A antibody (eBioscience, 25-7177-82). Acvrl1 was detected using a primary antibody (Abcam, EPR22985-125) followed by an ABflo 647-conjugated secondary antibody (ABclonal, AS060). Ki67 staining was performed using the Foxp3/Transcription Factor Staining Buffer Set (eBioscience, 00-5523-00) and anti-Ki67 antibody (eBioscience, 11-5698-82). Apoptosis was assessed with the Annexin V Apoptosis Detection Kit (eBioscience, 88-8005-72). Dead cells were excluded using Propidium Iodide (Sigma-Aldrich, 25535-16-4) or Ghost dye (Tonbo Biosciences, 13–0870). Flow cytometry data were acquired on a BD Celesta flow cytometer (BD Biosciences) and analyzed using FlowJo software (version 10.8.1, BD Biosciences).

qPCR analysis

RNA was extracted from CD300ld^{+} and CD300ld^{-} neutrophils using RNAiso Plus (Takara, 9109) and subsequently reverse-transcribed into cDNA with the HiScript III All-in-one RT SuperMix (Vazyme, R333-01). qPCR was conducted using the Taq Pro Universal SYBR qPCR Master Mix (Vazyme, Q712–02) in accordance with the manufacturer's protocol. The primer sequences used for qPCR are listed in table S5.

Immunofluorescence staining and analysis

Spleen, lung, and femur samples from EAE mice were first fixed in 4% paraformaldehyde. Femurs were subsequently decalcified in 0.5 M EDTA (pH 7.4) in PBS at 4°C for 2 days, followed by dehydration in 30% sucrose and embedding in Optimal Cutting Temperature (OCT) compound (Sakura, 4583). Sections were cut from OCT blocks at a thickness of 10 μm and mounted onto slides. Spleen and lung tissues were embedded in paraffin, and serial sections of 5 μm thickness were prepared. For immunofluorescence staining, sections were washed and blocked with 10% BSA for 1 hour at room temperature, followed by incubation with fluorochrome-conjugated antibodies against mouse Ly6G (BioLegend, 127615) and CD300ld (BioLegend, 139605) for 1 hour. After washing, sections were counterstained with DAPI for 5 minutes at room temperature, washed again, and mounted with coverslips using mounting medium. Imaging to analyze the distribution of neutrophil subsets was performed using a Nikon Eclipse Ti2 microscope.

Cell tracing assay

For intra-bone marrow injection, mice were anesthetized and the hair between the inguen and knee joint was removed. A 26-gauge needle was inserted through the patellar tendon into the tibial joint surface and guided carefully into the bone marrow cavity. Cells were labeled by injecting 100 μL of 40 μM CFSE (Invitrogen, C34554) into the marrow. For intra-spleen injection, a left subcostal incision exposed the spleen. 50 μL of 40 μM CellTrace Violet (Invitrogen, C34557) was injected at five sites to ensure even distribution. The abdominal muscle and skin were closed separately with sutures and wound clips. Five hours after dye injection, mice were sacrificed, and cells from bone marrow, blood, spleen, and lung were collected for flow cytometry analysis.

scRNA-seq data processing and clustering

Single-cell suspensions were prepared from the spleen, lung, and bone marrow of EAE mice at the peak stage. Single-cell libraries were generated using the Chromium Single Cell 3' v3 Reagent Kit (10x Genomics) according to the manufacturer's instructions and sequenced on an Illumina platform. Raw base call files were demultiplexed using Cell Ranger (version 9.0.1), and sequencing reads were aligned to the mouse reference transcriptome (GRCm39). After alignment, unique molecular identifiers (UMIs) and cell barcodes were filtered and corrected to generate gene-barcode count matrices. Count matrices from six samples generated in this study were imported into Seurat (version 5.3.0). Genes detected in fewer than three cells were excluded. Cells were retained if they expressed 300-5,000 genes and had < 10% mitochondrial gene content. Normalization and variance stabilization were performed with the SCTransform function (method = "glmGamPoi"), regressing out mitochondrial read percentages (vars.to.regress = "percent.mt"). Datasets were then integrated and batch-corrected using FindIntegrationAnchors and IntegrateData functions with default parameters, yielding a total of 75,832 cells after excluding red blood cells, endothelial and epithelial cells from the analysis. Cells were annotated with their original sample identifiers. Dimensionality reduction was carried out by principal component analysis on the top 3,000 highly variable genes. Clustering was performed using FindNeighbors function on the first 12 principal components, followed by FindClusters function with a resolution of 1.2. Cell type identities were assigned based on canonical marker gene expression.

Clustering analysis of neutrophils

Neutrophils from EAE mice identified in the initial dataset were extracted and subjected to a secondary round of dimensionality reduction using RunPCA and RunUMAP functions based on the first 10 principal components. Clustering was performed with the FindNeighbors and FindClusters functions at a resolution of 0.1. Cluster-specific marker genes were identified using FindAllMarkers function (min.pct = 0.25, logfc.threshold = 0.25), and the top 10 markers per cluster were visualized in a heatmap. The five resulting neutrophil clusters were further consolidated into three subsets based on shared transcriptional signatures. Data visualization was performed using the Seurat (version 5.3.0), SCP (version 0.5.6), scplotter (version 0.1.0), and ggplot2 (version 3.5.2) packages. scRNA-seq datasets from GSE130119 [23] and GSE118948 [24] were utilized to analyze neutrophils in the CNS of EAE mice. To compare neutrophil subsets with previously identified populations, scRNA-seq datasets were obtained from GSE243466 [3] and GSE266680 [6]. Raw UMI expression matrices were downloaded from the original studies and were processed according to the methods described in the original study. Cell type annotation was performed by transferring labels from a reference dataset to the query dataset using the FindTransferAnchors and TransferData functions in Seurat. For neutrophil subset analysis in naïve C57BL/6 mice, publicly available datasets from spleens (GSE186158 and GSE222784), lungs: (GSE220594 and PRJNA1099127), and bone marrow (GSE234000) [38–41] were projecting onto our datasets.

Scoring of biological processes

Gene signature and pathway activity analyses were performed using the AddModuleScore function in Seurat. “Neutrophil maturation” and “Neutrophil apoptosis” scores were calculated based on previously published gene sets [22], and the “MDSC signature” score was computed using a gene set curated in a prior study [4]. Other functional gene sets used to score neutrophils were compiled from previous studies [6] and relevant GO/GSEA terms, with the full gene list provided in table S1.

Developmental trajectory inference

Cell cycle states of neutrophil clusters were determined using the CellCycleScoring function implemented in Seurat, and the relative proportions of each state were visualized as pie charts. Neutrophil clusters identified in Seurat were used to generate a Monocle 3 object via the new_cell_data_set function. Cells were ordered along a pseudotime trajectory using the reduce_dimension function with the UMAP method and order_cells function. N0 neutrophils were designated as the root (initial stage) for trajectory inference. Pseudotime analysis of sub-clusters within N0, N1, and N2 neutrophils was performed using Slingshot function in SCP (version 0.5.6) package on the UMAP embedding from the Seurat object to infer lineage relationships and cell trajectories.

Correlation analysis of neutrophil subsets across tissues

For each neutrophil subset, scaled expression matrices were extracted from the SCT assay in Seurat, and average expression per tissue was calculated. Pearson correlation coefficients were computed to assess transcriptional similarity, and heatmaps were generated using the ComplexHeatmap (version 2.20.0) package with annotated correlation values.

Gene ontology analysis

DEGs were identified using the FindMarkers function in Seurat. The Wilcoxon rank-sum test (test.use = "wilcox") was used, and p-values were adjusted using the Bonferroni correction based on the total number of genes in the dataset. DEGs for each neutrophil subset were identified using $\log_2$ fold change > 2, adjusted p-value < 0.05, and min.pct = 0.1. For comparisons between EAE and naïve mice, DEGs were determined for each neutrophil subset separately across tissues (log2 fold change > 1, adjusted p-value < 0.05, min.pct = 0.1). To examine tissue-specific transcriptional differences among neutrophil subsets within EAE mice, DEGs were identified between tissues for each subset (log2 fold change > 0.5, adjusted p-value < 0.05, min.pct = 0.1). For comparisons between sub-clusters with N0, N1, and N2 neutrophils, DEGs were identified using the following criteria: log2 fold change > 0.5, adjusted p-value < 0.05, min.pct = 0.1. For comparisons between patients with MS and healthy controls, DEGs were determined for each neutrophil subset (log2 fold change > 0.3, adjusted p-value < 0.05, min.pct = 0.1). Gene Ontology enrichment analyses were performed using clusterProfiler (version 4.12.6) package.

Cell-cell communication analysis

To investigate intercellular signaling between neutrophil subsets and $CD4^+$ T cells during EAE, we used the CellChat (version 2.2.0) package. Single-cell expression data and cell-type annotations were used to

construct a CellChat object. The mouse ligand-receptor database (CellChatDB.mouse) was applied to map expressed ligands and receptors. Lowly expressed cells and interactions were filtered, and overexpressed genes and interactions were identified. Data were smoothed using a protein-protein interaction network (PPI.mouse) to project gene expression onto protein-level signaling. The number of interactions and their strengths were visualized using the netVisual_heatmap function. Key ligand-receptor pairs mediating interactions between N2 sub-clusters and $CD4^+$ T cell subsets were visualized using the netVisual_bubble function.

Graphs and statistical analyses

Data distribution was first assessed for normality. For comparisons between two groups, a two-tailed Student's t-test was used for samples with equal variance, while Welch's t-test was applied for samples with unequal variance. A paired t-test was used for matched samples. For comparisons involving more than two groups, one-way ANOVA with Tukey's multiple comparisons test was performed. Correlations were evaluated using the Pearson correlation coefficient. Data are presented as mean ± SEM, and statistical significance was defined as $P < 0.05$. All statistical analyses and graphical representations were performed using GraphPad Prism (version 10.4.0) and R (The R Project for Statistical Computing).

Declarations

Data and materials availability: The raw single-cell RNA sequencing data from spleens, lungs, and bone marrow have been deposited in the NCBI Sequence Read Archive under BioProject accession number PRJNA1356303.

Funding: This work is supported by the National Natural Science Foundation of China (32571054 and 82371350 to GY) and the Institute Digital Medicine grant at the City University of Hong Kong, grant number 9229501-13-YG.

Author contributions: Q.J.: Conceptualization, Methodology, Formal analysis, Investigation, Writing - Original Draft, Writing - Review & Editing, Visualization. G.Z.: Formal analysis, Data Curation. W.S.: Methodology, M.X.: Methodology, Q.L.: Writing - Review & Editing. G.Y.: Conceptualization, Writing - Review & Editing, Supervision, Project administration, Funding acquisition.

Competing interest statement: The authors declare that they have no competing interests.

Acknowledgments

Not applicable.

References

1. Wang, Y. *et al.* Cognate interaction-dependent pathogenicity of meningeal B cells drives neuroinflammation relapse. *Immunity* 58, 2256–2270. e2258 (2025).

2. Veglia, F. *et al.* Analysis of classical neutrophils and polymorphonuclear myeloid-derived suppressor cells in cancer patients and tumor-bearing mice. *Journal of Experimental Medicine* 218, e20201803 (2021).
3. Ng, M. S. *et al.* Deterministic reprogramming of neutrophils within tumors. *Science* 383, eadf6493 (2024).
4. Alshetaiwi, H. *et al.* Defining the emergence of myeloid-derived suppressor cells in breast cancer using single-cell transcriptomics. *Science immunology* 5, eaay6017 (2020).
5. Ugolini, A. *et al.* Functional reprogramming of neutrophils within the brain tumor microenvironment by hypoxia-driven histone lactylation. *Cancer Discovery* 15, 1270–1296 (2025).
6. Cerezo-Wallis, D. *et al.* Architecture of the neutrophil compartment. *Nature* 649, 1003–1012, doi:10.1038/s41586-025-09807-0 (2026).
7. Chang, X., Liu, Y., Qiu, J. & Hua, K. Role of Neutrophils in Homeostasis and Diseases. *MedComm* 6, e70390 (2025).
8. Wang, X., Qiu, L., Li, Z., Wang, X.-Y. & Yi, H. Understanding the multifaceted role of neutrophils in cancer and autoimmune diseases. *Frontiers in immunology* 9, 2456 (2018).
9. Knier, B. *et al.* Myeloid-derived suppressor cells control B cell accumulation in the central nervous system during autoimmunity. *Nature immunology* 19, 1341–1351 (2018).
10. Jiang, Q., Duan, J., Van Kaer, L. & Yang, G. The Role of Myeloid-Derived Suppressor Cells in Multiple Sclerosis and Its Animal Model. *Aging and Disease* 15, 1329 (2024).
11. Fresneda Alarcon, M., McLaren, Z. & Wright, H. L. Neutrophils in the pathogenesis of rheumatoid arthritis and systemic lupus erythematosus: same foe different MO. *Frontiers in immunology* 12, 649693 (2021).
12. Ballesteros, I. *et al.* Co-option of neutrophil fates by tissue environments. *Cell* 183, 1282–1297. e1218 (2020).
13. Ng, L. G. *et al.* From complexity to consensus: A roadmap for neutrophil classification. *Immunity* 58, 1890–1903 (2025).
14. Rumble, J. M. *et al.* Neutrophil-related factors as biomarkers in EAE and MS. *Journal of Experimental Medicine* 212, 23–35 (2015).
15. Glenn, J. D., Liu, C. & Whartenby, K. A. Frontline Science: Induction of experimental autoimmune encephalomyelitis mobilizes Th17-promoting myeloid derived suppressor cells to the lung. *Journal of Leukocyte Biology* 105, 829–841 (2019).
16. Kular, L. The lung-brain axis in multiple sclerosis: Mechanistic insights and future directions. *Brain, Behavior, & Immunity-Health* 38, 100787 (2024).
17. Saito, E. *et al.* Modulating lung immune cells by pulmonary delivery of antigen-specific nanoparticles to treat autoimmune disease. *Science advances* 6, eabc9317 (2020).
18. Hosang, L. *et al.* The lung microbiome regulates brain autoimmunity. *Nature* 603, 138–144 (2022).

19. Wegner, A., Verhagen, J. & Wraith, D. C. Myeloid-derived suppressor cells mediate tolerance induction in autoimmune disease. *Immunology* 151, 26–42 (2017).
20. Ioannou, M. *et al.* Crucial role of granulocytic myeloid-derived suppressor cells in the regulation of central nervous system autoimmune disease. *The Journal of Immunology* 188, 1136–1146 (2012).
21. Zhang, F. *et al.* Neutrophil diversity and function in health and disease. *Signal transduction and targeted therapy* 9, 343 (2024).
22. Xie, X. *et al.* Single-cell transcriptome profiling reveals neutrophil heterogeneity in homeostasis and infection. *Nature immunology* 21, 1119–1133 (2020).
23. Wheeler, M. A. *et al.* MAFG-driven astrocytes promote CNS inflammation. *Nature* 578, 593–599, doi:10.1038/s41586-020-1999-0 (2020).
24. Jordão, M. J. C. *et al.* Single-cell profiling identifies myeloid cell subsets with distinct fates during neuroinflammation. *Science* 363, doi:10.1126/science.aat7554 (2019).
25. Roman, B. L. & Hinck, A. P. ALK1 signaling in development and disease: new paradigms. *Cellular and Molecular Life Sciences* 74, 4539–4560 (2017).
26. Wang, C. *et al.* CD300ld on neutrophils is required for tumour-driven immune suppression. *Nature* 621, 830–839 (2023).
27. Evrard, M. *et al.* Developmental analysis of bone marrow neutrophils reveals populations specialized in expansion, trafficking, and effector functions. *Immunity* 48, 364–379. e368 (2018).
28. Shan, Z. G. *et al.* FasL + PD-L2 + identifies a novel immunosuppressive neutrophil population in human gastric cancer that promotes disease progression. *Advanced Science* 9, 2103543 (2022).
29. Podaza, E. *et al.* Chronic lymphocytic leukemia cells increase neutrophils survival and promote their differentiation into CD16highCD62Ldim immunosuppressive subset. *International Journal of Cancer* 144, 1128–1134 (2019).
30. Meng, Y. *et al.* Immunosuppressive CD10 + ALPL+ neutrophils promote resistance to anti-PD-1 therapy in HCC by mediating irreversible exhaustion of T cells. *Journal of hepatology* 79, 1435–1449 (2023).
31. Veglia, F., Perego, M. & Gabrilovich, D. Myeloid-derived suppressor cells coming of age. *Nature immunology* 19, 108–119 (2018).
32. Guo, R., Xie, X., Ren, Q. & Liew, P. X. New insights on extramedullary granulopoiesis and neutrophil heterogeneity in the spleen and its importance in disease. *Journal of Leukocyte Biology* 117, qiae220 (2025).
33. Reichard, A., Wanner, N., Farha, S. & Asosingh, K. Hematopoietic stem cells and extramedullary hematopoiesis in the lungs. *Cytometry Part A* 103, 967–977 (2023).
34. De Filippo, K. & Rankin, S. M. CXCR 4, the master regulator of neutrophil trafficking in homeostasis and disease. *European journal of clinical investigation* 48, e12949 (2018).
35. Hong, C.-W. Current understanding in neutrophil differentiation and heterogeneity. *Immune network* 17, 298 (2017).

36. Adams, W., Espicha, T. & Estipona, J. Getting your neutrophil: neutrophil transepithelial migration in the lung. *Infection and Immunity* 89, 10.1128/iai. 00659 – 00620 (2021).
37. Luan, Y. *et al.* Wnt5 controls splenic myelopoiesis and neutrophil functional ambivalency during DSS-induced colitis. *Cell reports* 43 (2024).
38. Jiao, A. *et al.* Single-cell sequencing reveals the evolution of immune molecules across multiple vertebrate species. *Journal of Advanced Research* 55, 73–87 (2024).
39. Pham, H. T. T. *et al.* Neutrophil metalloproteinase driven spleen damage hampers infection control of trypanosomiasis. *Nature Communications* 14, 5418 (2023).
40. Wang, H. *et al.* High mortality of Acinetobacter baumannii infection is attributed to macrophage-mediated induction of cytokine storm but preventable by naproxen. *EBioMedicine* 108 (2024).
41. Xu, Q. *et al.* Molecular mechanisms underlying the high mortality of hypervirulent Klebsiella pneumoniae and its effective therapy development. *Signal transduction and targeted therapy* 8, 221 (2023).
42. Gong, Z. *et al.* Immunosuppressive reprogramming of neutrophils by lung mesenchymal cells promotes breast cancer metastasis. *Science immunology* 8, eadd5204 (2023).
43. Lilja, S. *et al.* Multi-organ single-cell analysis reveals an on/off switch system with potential for personalized treatment of immunological diseases. *Cell Reports Medicine* 4 (2023).
44. Akama-Garren, E. H. & Carroll, M. C. Lupus susceptibility loci predispose mice to clonal lymphocytic responses and myeloid expansion. *The Journal of Immunology* 208, 2403–2424 (2022).
45. Hoover, P. J. *et al.* A human-mouse atlas of intrarenal myeloid cells identifies conserved disease-associated macrophages in lupus nephritis. *Journal of Experimental Medicine* 222, e20241873 (2025).
46. Shi, K. *et al.* Bone marrow hematopoiesis drives multiple sclerosis progression. *Cell* 185, 2234–2247. e2217 (2022).
47. Capucetti, A., Albano, F. & Bonecchi, R. Multiple roles for chemokines in neutrophil biology. *Frontiers in immunology* 11, 1259 (2020).
48. Drifte, G., Dunn-Siegrist, I., Tissières, P. & Pugin, J. Innate immune functions of immature neutrophils in patients with sepsis and severe systemic inflammatory response syndrome. *Crit Care Med* 41, 820–832, doi:10.1097/CCM.0b013e318274647d (2013).
49. Fraccarollo, D. *et al.* Expansion of CD10neg neutrophils and CD14 + HLA-DRneg/low monocytes driving proinflammatory responses in patients with acute myocardial infarction. *eLife* 10, e66808, doi:10.7554/eLife.66808 (2021).
50. Wang, L. *et al.* ROS-producing immature neutrophils in giant cell arteritis are linked to vascular pathologies. *JCI insight* 5, e139163 (2020).
51. Saqib, M. *et al.* Pathogenic role for CD101-negative neutrophils in the type I interferon-mediated immunopathogenesis of tuberculosis. *Cell reports* 44 (2025).

52. Nobs, S. P. & Kopf, M. Tissue-resident macrophages: guardians of organ homeostasis. *Trends in immunology* 42, 495–507 (2021).
53. Omdahl, K. I. *et al.* Organ-specific microenvironments drive divergent T cell evolution in acute graft-versus-host disease. *Science Translational Medicine* 17, eads1298 (2025).
54. Crinier, A. *et al.* High-dimensional single-cell analysis identifies organ-specific signatures and conserved NK cell subsets in humans and mice. *Immunity* 49, 971–986. e975 (2018).
55. Tellier, J. *et al.* Unraveling the diversity and functions of tissue-resident plasma cells. *Nature immunology* 25, 330–342 (2024).
56. Jiang, Q. *et al.* Altered T cell development in an animal model of multiple sclerosis. *Experimental Neurology* 371, 114579 (2024).

Figures

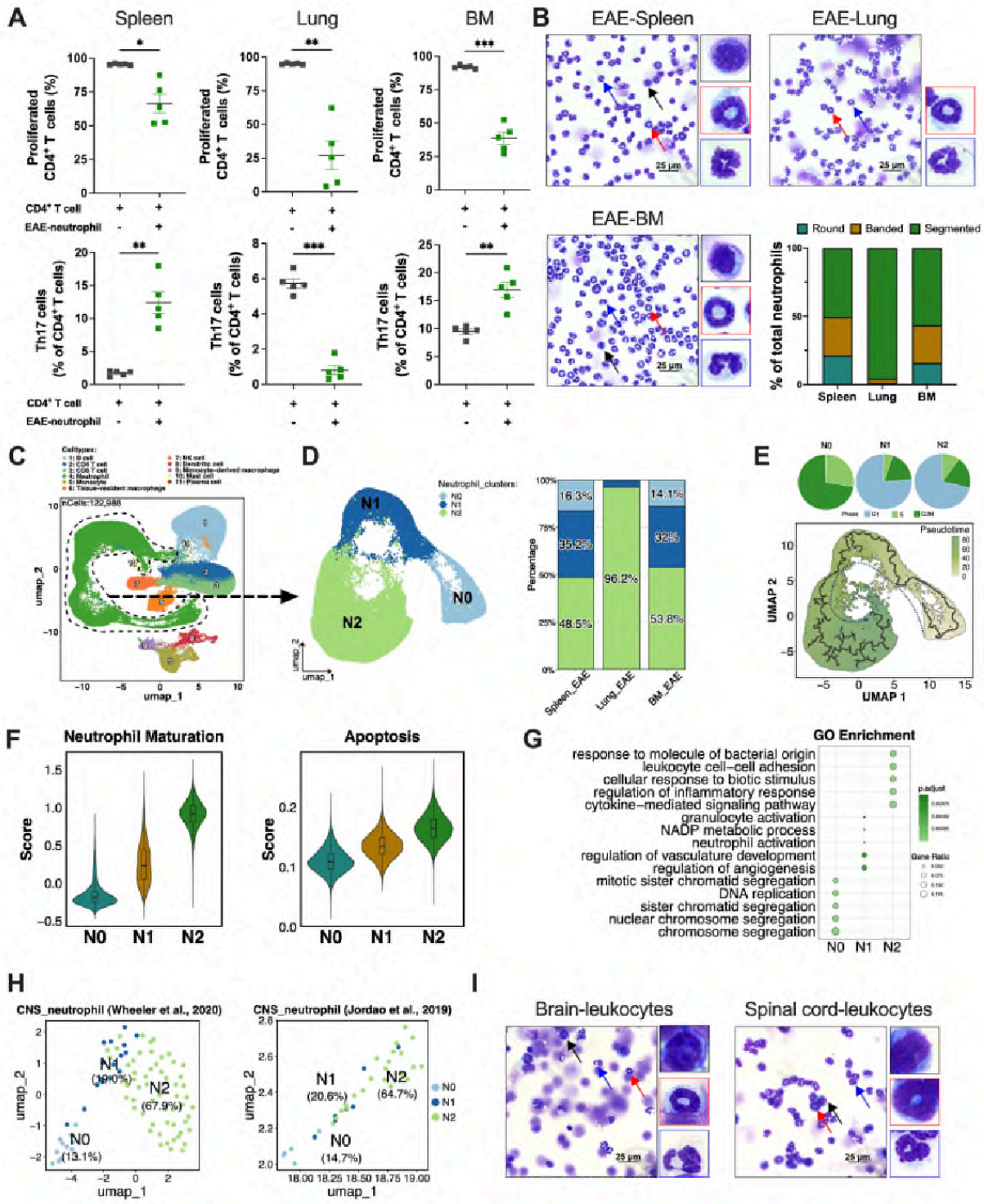


Figure 1

Tissue-specific functional, morphological, and transcriptional heterogeneity of neutrophils in EAE. (A) CFSE-labeled naïve CD4⁺ T cells were co-cultured with neutrophils isolated from the spleen, lung, or bone marrow of EAE mice at the peak stage with anti-CD3e and anti-CD28 antibodies. CD4⁺ T cell proliferation was assessed by flow cytometry (n = 5) (top). In parallel, naïve CD4⁺ T cells were co-cultured with neutrophils from the same tissues under Th17-polarizing conditions, and the proportion of Th17 cells

was measured by flow cytometry (n = 5) (bottom). **(B)** Representative neutrophil morphologies in the spleen, lung, and bone marrow of EAE mice at peak stage. Quantification of neutrophils with round, banded, or segmented nuclei in each tissue is shown. Data represent the average of five mice, with three independent fields of view analyzed per mouse. **(C)** UMAP plot showing major immune cell types from single-cell RNA sequencing of spleen, lung, and bone marrow samples of EAE mice at peak stage (day 17 post-immunization). **(D)** UMAP plot showing three neutrophil subsets (left). Neutrophil subset proportions in the spleen, lung, and bone marrow of EAE mice (right). **(E)** Pie charts showing the proportion of each neutrophil subset predicted to be in the G1, S, or G2M phase of the cell cycle (top). Monocle trajectory analysis using UMAP embedding of combined neutrophils from EAE mice (bottom). **(F)** Violin plot of neutrophil maturation (left) and apoptosis (right) scores for each neutrophil subset. **(G)** Gene Ontology (GO) analysis of differentially expressed genes (DEGs) for each subset. **(H)**UMAP plot showing three neutrophil subsets in the CNS of EAE mice. **(I)** Representative neutrophil morphologies in the CNS of EAE mice. Data are means ± SEM. Statistical significance was assessed using Welch's t-test (A). $*P < 0.05$, $**P < 0.01$, and $***P < 0.001$.

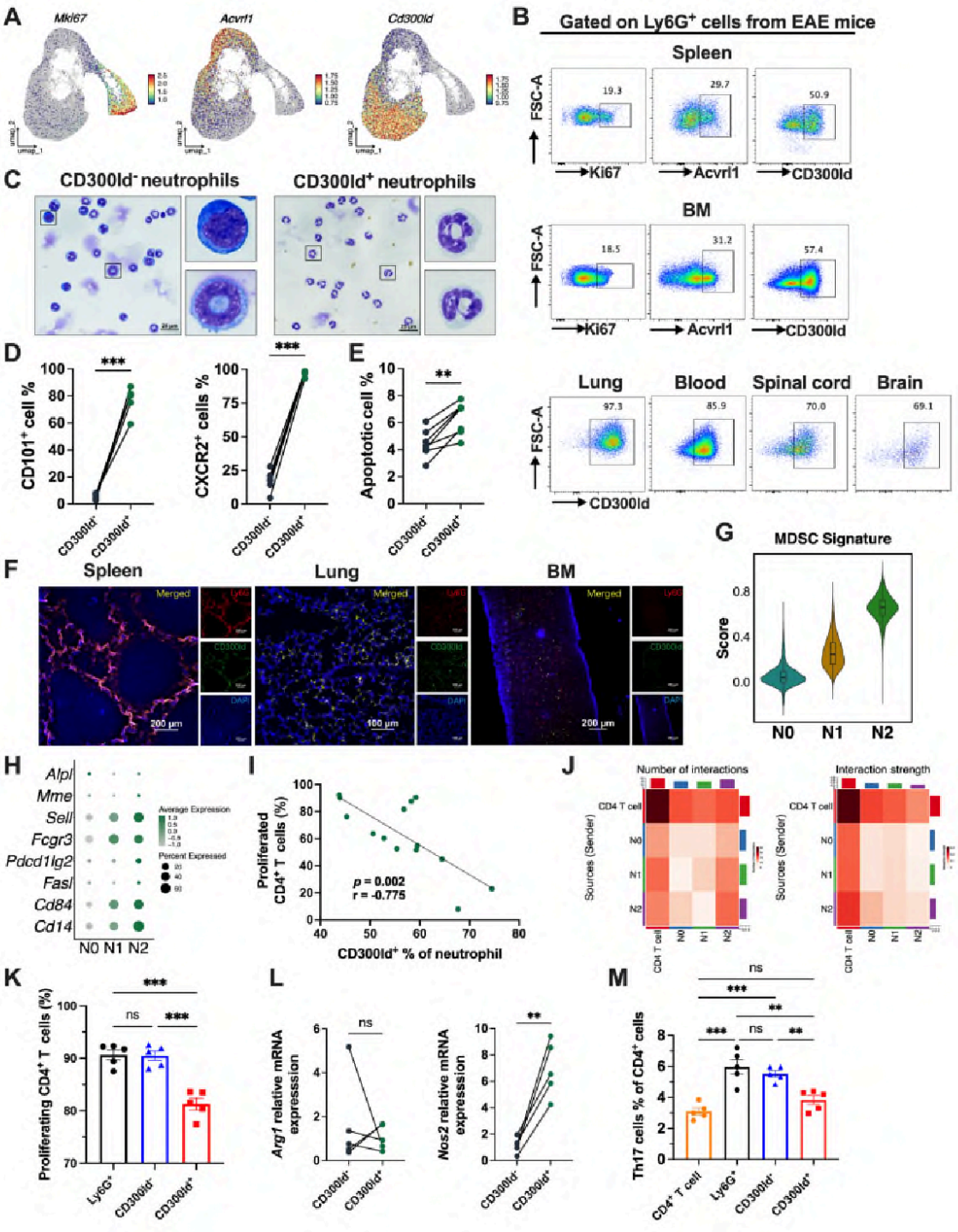


Figure 2

Defining markers and divergent functional roles of neutrophil subsets in EAE. (A) UMAP plots showing expression of *Mki67*, *Acvrl1*, and *Cd300ld* in neutrophils from EAE mice. **(B)** Flow cytometric analyses of Ki67, Acvrl1, and CD300ld expression on neutrophils from spleen, lung, bone marrow, blood, brain and spinal cord of EAE mice at peak stage. **(C)** Representative morphologies of $CD300ld^-$ and $CD300ld^+$ neutrophils from the spleen of EAE mice at peak stage. **(D)** Proportions of $CD101^+$ (left) and $CXCR2^+$

(right) cells in CD300ld$^-$ and CD300ld$^+$ neutrophils (n=6). **(E)** Proportion of apoptotic cells in CD300ld$^-$ and CD300ld$^+$ neutrophils (n=7). **(F)** Spatial localization of neutrophil subsets in the spleen, lung and bone marrow of EAE mice at peak stage. **(G)** Violin plot depicting MDSC signature scores for each neutrophil subset. **(H)** Dot plot showing scaled expression of previously identified markers for immunosuppressive neutrophils. **(I)** Correlation between the frequency of CD300ld$^+$ neutrophils and CD4$^+$ T cell proliferation in *in vitro* co-culture (n=14). **(J)** Heatmap showing the number of interactions and interaction strength between CD4$^+$ T cells and neutrophil subsets from EAE mice. **(K)** Proliferation of CFSE-labeled naïve CD4$^+$ T cells co-cultured with Ly6G$^+$, CD300ld$^-$ Ly6G$^+$, and CD300ld$^+$ Ly6G$^+$ neutrophils isolated from the spleens of EAE mice at the peak stage. **(L)** qPCR analysis of *Arg1* (left) and *Nos2* (right) expression in CD300ld$^-$ and CD300ld$^+$ Ly6G$^+$ neutrophils (n=5). **(M)** Naïve CD4$^+$ T cells were co-cultured with/without Ly6G$^+$, CD300ld$^-$ Ly6G$^+$, and CD300ld$^+$ Ly6G$^+$ neutrophils isolated from the spleens of EAE mice under Th17-polarizing conditions, and the percentage of Th17 cells was measured by flow cytometry (n=5). Data are means ± SEM. Statistical significance was assessed using paired t-test (D, E, and L), simple linear regression (I), and one-way ANOVA with Tukey's multiple comparison test (K and M). $^{**}P < 0.01$, and $^{***}P < 0.001$.

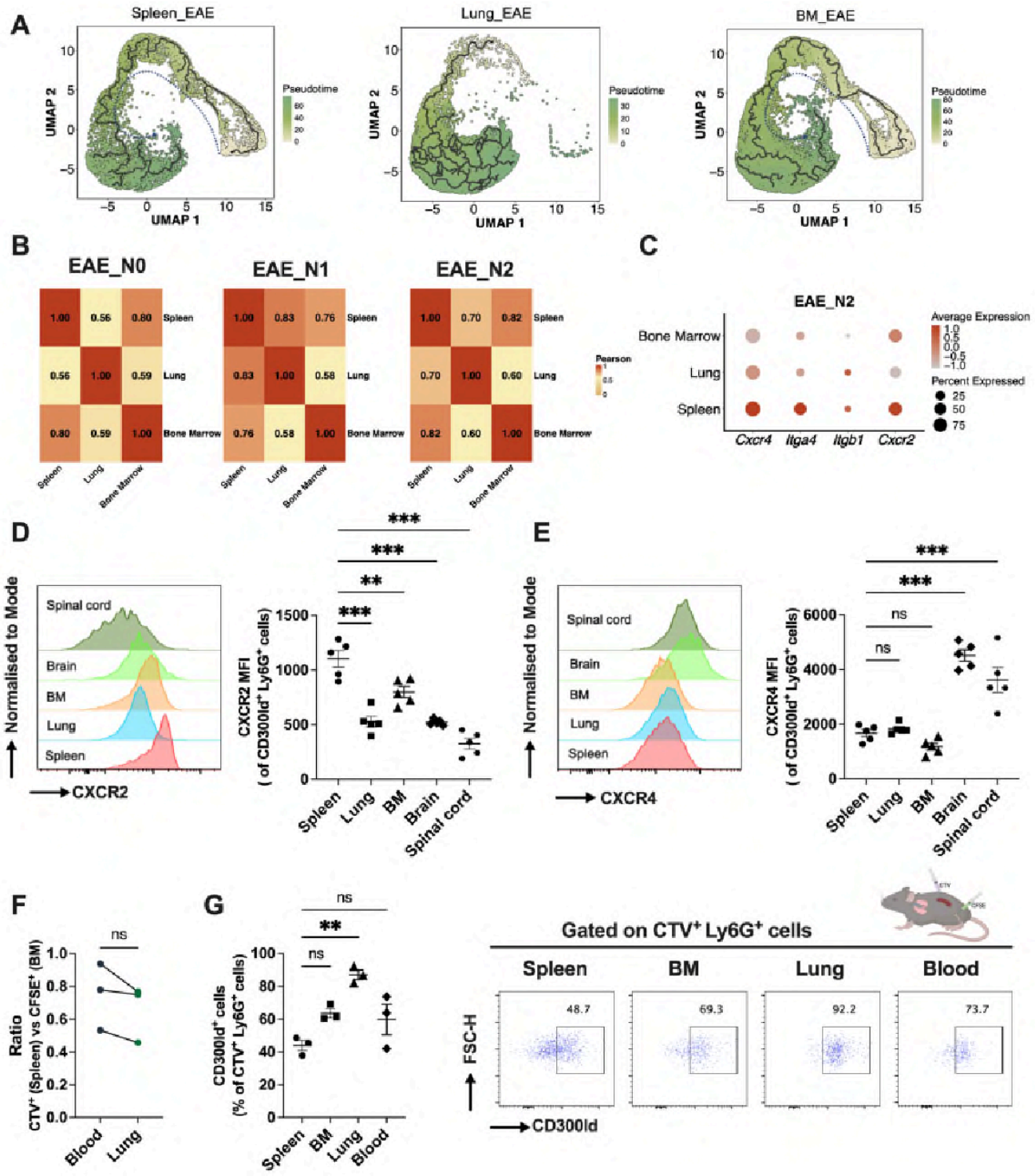


Figure 3

Contribution of splenic extramedullary granulopoiesis to circulating and tissue-resident neutrophil subsets in EAE. (A) Monocle trajectory analyses using UMAP embedding of neutrophils from the spleen, lung, and bone marrow of EAE mice. **(B)** Correlation matrices generated with Pearson's correlation coefficients representing similarities in gene expression between neutrophil subsets in EAE mice. **(C)** Dot plot displaying the scaled expression of tissue-homing markers in N2 neutrophils from EAE mice. **(D)**

Representative histograms and quantification of CXCR2 expression in CD300ld^{+}neutrophils from spleen, lung, bone marrow, brain, and spinal cord of EAE mice (n = 5) analyzed by flow cytometry. **(E)** CXCR4 expression in CD300ld^{+} neutrophils from the same tissues of EAE mice (n = 5) measured by flow cytometry. **(F)** Ratio of spleen- to bone marrow-derived neutrophils infiltrating the blood and lungs of EAE mice (n = 3). **(G)** Proportion of CD300ld^{+} neutrophils within spleen-derived neutrophils that infiltrated the bone marrow and lungs of EAE mice (n = 3). Data are means ± SEM. Statistical significance was assessed using and one-way ANOVA with Tukey's multiple comparisons test (D, E, and G) and a paired t-test (F). ***P*< 0.01 and ****P* < 0.001.

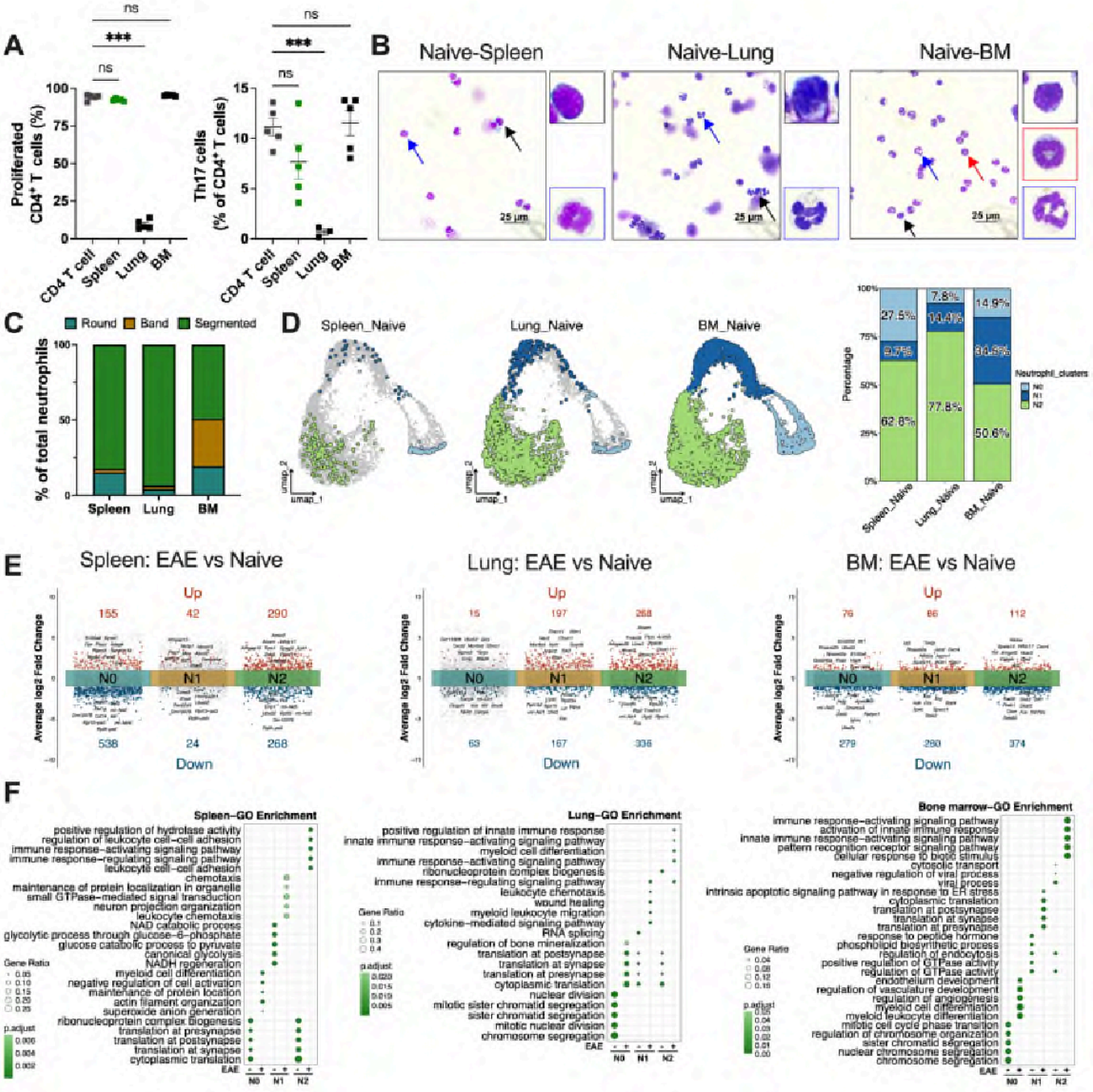


Figure 4

Neutrophil subset characterization in naïve mice and their reprogramming during EAE. (A) CFSE-labeled naïve $CD4^+$ T cells were co-cultured with neutrophils isolated from the spleen, lung, or bone marrow of naive mice with anti-CD3e and anti-CD28 antibodies. $CD4^+$T cell proliferation was assessed by flow cytometry (n = 5) (left). In parallel, naïve $CD4^+$T cells were co-cultured with neutrophils from the same tissues under Th17-polarizing conditions, and the proportion of Th17 cells was measured by flow cytometry (n = 3-5) (right). **(B)** Representative neutrophil morphologies in the spleen, lung, and bone marrow of naive mice. **(C)**Quantification of neutrophils with round, banded, or segmented nuclei in each tissue is shown. Data represent the average of five mice, with three independent fields of view analyzed per mouse. **(D)** Tissue distribution and proportions of the three previously identified neutrophil subsets in the spleen, lung, and bone marrow of naive mice. **(E)** Volcano plots showing DEGs between EAE and naïve conditions in each neutrophil subset. **(F)** GO analysis of subset-specific DEGs between EAE and naïve conditions for each tissue. Data are means ± SEM. Statistical significance was assessed one-way ANOVA with Tukey's multiple comparison test (A). ***$P < 0.001$.



Figure 5

Microenvironment-driven transcriptional and functional reprogramming of neutrophil subsets in EAE. (A) GO analysis of DEGs between tissues within each neutrophil subset from EAE mice. **(B)** Heatmap showing the expression of genes associated with immunosuppression in N2 neutrophils across different tissues of EAE mice. **(C)** CD300ld expression in $CD300ld^+$ neutrophils from various tissues of EAE mice (n=5). **(D)** The proportion of $PD\text{-}L1^+$ cells in $CD300ld^+$ neutrophils from various tissues of EAE mice (n=5). **(E)** CD300ld expression in infiltrating $CD300ld^+$ neutrophils derived from bone marrow (left) or spleen (right) (n=3) in *in vivo* cell tracing assay. Data are means ± SEM. Statistical significance was assessed using one-way ANOVA with Tukey's multiple comparison test (C-E). *$P < 0.05$, and ***$P < 0.001$.



Figure 6

Identification and characterization of sub-clusters within N0, N1, and N2 neutrophils. (A) UMAP visualization of three transcriptionally distinct sub-clusters within N0 neutrophils. **(B)** GO analysis of DEGs for each N0 sub-cluster. **(C)** Proportions of N0 sub-clusters across spleen, lung, and bone marrow in naïve and EAE mice. **(D)**UMAP visualization of three sub-clusters within N1 neutrophils. **(E)** GO analysis of DEGs for each N1 sub-cluster. **(F)** Proportions of N1 sub-clusters in spleen, lung, and bone marrow of naïve and EAE mice. **(G)**UMAP visualization of seven sub-clusters within N2 neutrophils. **(H)** GO analysis of DEGs for each N2 sub-cluster. **(I)** Proportions of N2 sub-clusters in spleen, lung, and bone marrow of naïve and EAE mice. **(J)**Functional scoring of N2 neutrophil sub-clusters for key biological processes. **(K)** Comparison of neutrophil sub-clusters identified in this study with populations reported by Cerezo-Wallis et al., with our labels mapped onto their dataset.



Figure 7

Neutrophil subsets in other animal models of autoimmune diseases and in patients with multiple sclerosis. (A) UMAP visualization of neutrophil subsets from the spleen and joint of CIA mice. Dot plot showing scaled expression of *Mki67*, *Acvrl1*, and *Cd300ld* across neutrophil subsets. **(B)** UMAP visualization of neutrophil subsets from the spleen and kidney of SLE.yaa mice. Dot plot showing scaled expression of *Mki67*, *Acvrl1*, and *Cd300ld* across neutrophil subsets. **(C)** Proportions of neutrophil subsets in CIA (left) and SLE (right) mice. **(D)** UMAP visualization of neutrophil subsets from healthy controls and patients with MS (left). Pie charts showing the proportion of each neutrophil subset predicted to be in the G1, S, or G2M phase of the cell cycle (right). **(E)** Proportion of neutrophil subsets in each individual. **(F)** GO enrichment analysis of subset-specific DEGs between healthy controls and patients with MS.

Supplementary Files

This is a list of supplementary files associated with this preprint. Click to download.

- 03102026SupplementarytablesV6.xlsx
- 03102026SI.docx